

Uniformly spaced nanoscale cracks in nanoparticle films deposited by convective assembly

Alexander L. Weldon*, Kedar Joshi*, Alexander Routh† and James F. Gilchrist*

* Department of Chemical Engineering, Lehigh University, Bethlehem, PA, 18015 USA

† BP Institute and Department of Chemical Engineering and Biotechnology, University of Cambridge, Pembroke Street, Cambridge CB2 3RA, UK

Abstract

Rapid convective deposition is used to assemble nanoparticle coatings from suspension, with controllable thickness. Varying film thickness generates stress-induced linear cracks with highly monodisperse spacing. Film thickness is controlled through mechanical means, suspension volume fraction, and the use of applied thermal gradients. These cracks extend in the deposition direction, and a uniform crack spacing from 2-160 μm is observed. The nanoparticle film thickness is the relevant length scale for hydrodynamic flow, and films will crack with this spacing, in a characteristic manner to minimize the system energy and capillary stresses. As expected from this energy minimization problem and relevant theory, the correlation between coating thickness and crack spacing is highly linear. Because this process is continuous, continuous cracks have potential as a high-throughput method of fabricating nanoscale channels for microfluidics and MEMS.

Introduction and background

There is a strong interest in the controllable formation of defect-free, uniform nanoparticle thin films.¹⁻³ ordered particle layers and thin films have found enormous use recently in industries spanning a huge array of fields. Fields impacted include photonics,⁴⁻⁹ lithography,^{7,10,11} ceramics,¹⁰ sensors,¹²⁻¹⁶ diagnostic platforms,¹⁷⁻²⁰ membranes,²¹⁻²⁵ biocompatible surfaces^{14,26} and making Janus particles²⁷⁻²⁹. Extensive efforts have focused on the VOC-free formation of latex coatings³⁰. There is a significant drive to move towards aqueous systems in order to minimize the environmental impact of these coatings. In addition, it is critical that the drying process in forming these coatings does not result in stresses that result in buckling and cracks because of their inherent non-uniformity across films as well as their random cracking patterns.

On the other hand, there are several uses for uniform cracks as nanoscale channels³¹ and as optical devices^{32,33} that provide separate length scales from the nanoparticle diameter to the film thickness to the spacing between cracks. Previous efforts³⁴ have investigated batch-wise drop drying techniques that have the potential of creating nearly parallel cracks over small areas. Three drawbacks to this technique are the limited span of the cracks, the inability to dynamically alter crack spacing, and finally the hindrance to scaling up the process to roll-to-roll processing for commercial applications. Han et al. showed such cracks can be formed at micron scale³⁴, which opened a new technique to fabricate lithography detail structure. Lithographic processes are costly and time consuming and the additional benefit of using nanoparticle films is the channels are already embedded in a porous medium, which could be used as part of the microfluidic platform or filled in by melting or back-filling the nanoparticle film. As first

steps toward overcoming these challenges, this study serves as a platform that demonstrates a robust understanding of cracking dynamics during convective deposition that give a breadth of processing conditions that can result in uniformly spaced parallel cracks.

Previous efforts have aimed to characterize varying deformation mechanisms and evolving stresses in these drying systems as a function of temperature and evaporation flux^{30,35}. In particular, nanoparticle films are susceptible to micro- or macroscale cracking—under some conditions these cracks can exhibit highly monodisperse spacing.^{36–39} The formation of latex films from bulk suspension is explained through three sequential steps.⁴⁰ Initially, the fluid evaporates and forces particles into a close-packed microstructure. Next, the particles deform as they contact one another and transition to an increasingly dense arrangement. Finally, polymer chains reptate and interdiffuse resulting in a homogeneous, and mechanically stronger, film. Cracking is a result of these capillary forces. As the fluid evaporates, it generates tremendous drying stresses that compress the film.^{36,41} Cracks form in order to release these stresses. Dufresne et al., validate these conclusions by showing that cracking films are wetted except at the cracks themselves.⁴² For rigid particles, deformation resulting from drying stresses is minimal, thus these mechanisms do not apply.

Routh et al., provide extensive modeling and theory to describe crack formation in drying of nanoparticle suspensions.³⁶ Solvent evaporation near the drying front leads to a consolidation of particles and increased volume fraction. This will generate a pressure drop and increased fluid flow through the higher-density system. Solvent pressure in the system can be calculated through Darcy's Law as given below. (equation 1)

$$\nabla p = -\frac{\mu}{k_p} u \quad (1)$$

Where ∇p is pressure gradient in deposition direction, μ is solvent viscosity, k_p is the permeability of a packed bed of particles, and u is the velocity of the fluid. Geometrically, the maximum capillary pressure drop for a close packed monodisperse particle array will be, $\Delta p = 10\gamma/a$. Here, γ is surface tension and a is the particle radius.

This maximum capillary pressure is used to extrapolate a relaxation length scale, X . Using the Carmen-Kozeny equation which determines the permeability through close pack structure (equation 2).

$$k_p = \frac{2a^2(1-\phi_m)^2}{75\phi_m^2} \quad (2)$$

With ϕ_m is the particle volume fraction in the deposited film. Finally, an expression for velocity can be expressed as an evaporation rate, J_e with a scaled length to height ratio, L/h , of the dried film. Thus the characteristic velocity will be:

$$u = \left(\frac{\gamma}{3\eta J_e} \right)^{1/4} J_e \quad (3)$$

Substituting (2) and (3) into Darcy's Law and equating it to the pressure drop allows the derivation of an expression for the relaxation length scale X for flow away from a crack face.

$$X \approx \frac{20a(1-\phi_m)^2}{75\mu\phi_m^2} \left(\frac{3\eta\gamma^3}{J_e^3} \right)^{1/4} \quad (4)$$

Replacing this length scale with a capillary length will yield a characteristic pressure, which, scaled by capillary pressure drop, yields a dimensionless pressure term which can characterize fluid flow through the higher volume fraction consolidated particle array.

$$p_{cap} = \frac{20a(1-\phi_m)^2}{75\mu\phi_m^2 h} \left(\frac{3\gamma\eta}{J_e} \right)^{1/2} \quad (5)$$

Under moderate capillary pressures, the fluid can flow as needed through the thin film to the compacted particle array. However, as the capillary pressure reaches its maximum, replacement fluid can no longer flow to compensate for that lost due to evaporation. It is this hydrodynamic length scale, the capillary pressure-driven distance the fluid must flow to compensate for that lost to evaporation that controls the onset and evolution of cracking. In particular, capillary forces put the particle thin film under tension. As these stresses grow with increasing evaporation, the system seeks to minimize its capillary forces and its energy. Upon the formation of “cracks,” fluid recedes into the particle thin film and the system energy relaxes.

The supposition that crack spacing scales with thin film thickness, and resulting increased drying stresses, has been validated experimentally. Routh et al., 2004 use Vernier calipers to measure the macroscale crack spacing and film thickness in latex and silica systems.³⁶ Crack spacing in these systems spans 0.1 to 10 mm and film thickness spans 10 to 1000 μm . Cracks form with a highly monodisperse spacing as a result of the characteristic hydrodynamic distance that fluid must flow upon the onset of cracks. These data suggest a scaling of crack spacing with film thickness over a pair of particle chemistries and a range of particle sizes. Routh et al. scale crack spacing, y , by X ,³⁶ and

find that they scale with $p_{cap}^{-0.8}$. They expect the trend to be linear, and attribute an imperfect fit to an overestimate of the maximum capillary pressure.

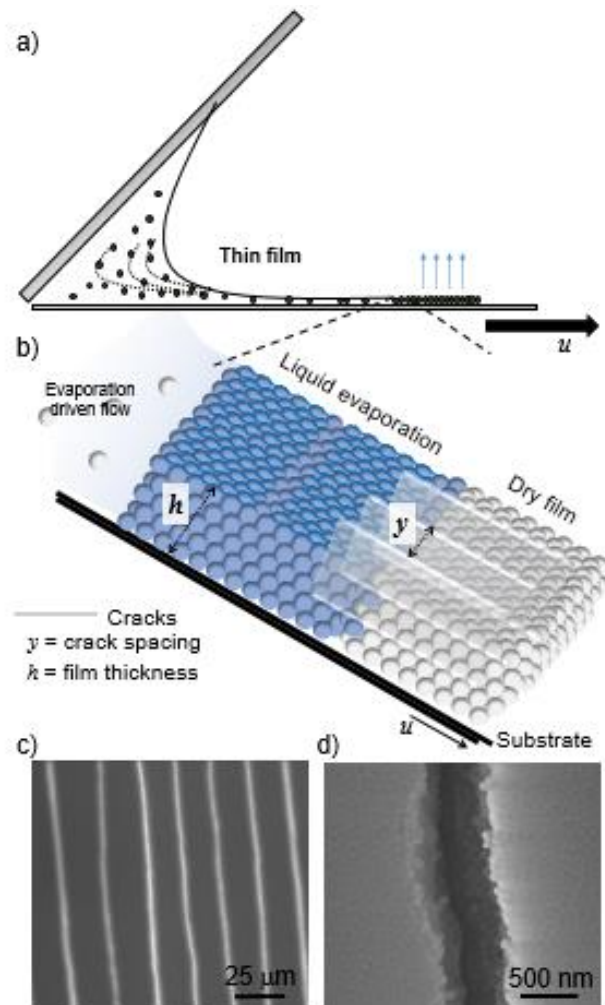


Figure 1 a) Convective deposition assembly setup, b) particles then assemble themselves at the packing front and liquid flows through this porous media to compensate for evaporation losses. Compressive stresses developed due to capillary forces and results in formation of cracks. C, d) Cracks at different magnification formed during deposition of 80 nm SiO_2 particles.

One of the methods for the deposition of uniform particle layers is rapid convective deposition (Figure 1a). Other methods include spin coating^{43–45}, gravity settling^{25,46}, electrophoretic assembly^{13,47,48}. Convective deposition is similar to vertical deposition, also known as dip coating^{49–52}, however evaporation of the liquid phase of a suspension

drives fluid to flow into a thin film where particles align on a surface due to either capillary forces⁵³ or increased volume fraction.^{54–58} Rapid convective deposition can deposit submonolayer, monolayer, and multilayer morphologies comprised of particles ranging from 10 nm to multiple microns. Spherical particles are typically deposited, but the process is by no means limited in this respect.

In this work we have observed the formation of highly uniform, parallel cracks in nanoparticle films of a critical thickness (Figure 1c). These cracks are aligned parallel with the direction of the film formation and the spacing of the cracks is variable with the final film thickness. The principle of controllably depositing particles from suspension is not a new concept. Dimitrov and Nagayama provide seminal work as to the controllable deposition of a particle monolayer.^{59–61} For a single-component suspension, they derived the relationship between volume fraction and deposition speed for an advancing crystal on a substrate. This mass balance results from equating solvent evaporation to flow in the thin film as shown in equation (6).

$$h = \frac{\beta J_e \ell}{u} \left(\frac{\phi}{\phi_m (1 - \phi)} \right) \quad (6)$$

u is substrate velocity and equal to the velocity of the advancing crystal front, J_e is solvent evaporation rate m/s, ℓ is evaporation length, h is thin film height, ϕ and ϕ_m are suspension volume fraction in solution and within the deposited thin film respectively, and β describes particle-surface interactions. For the special case of the deposition of a particle monolayer, $u = v_{mono}$ and $h = 2a$. Assumptions in implementing this equation include that the bulk suspension volume fraction equals particle volume fraction near the advancing crystal front and that when particle-surface interactions are strongly repulsive $\beta \approx 1$, but it is very sensitive to surface charge of particles and can show significant effect

on assembly⁶². This work concerns the assembly of multilayer coatings. slower deposition speed will yield thicker, multilayer, coatings.¹⁷ The assembly of multilayer thin films will increase film height, h , and consequently control crack formation. Also, obviously, increased suspension volume fraction will yield the formation of thicker coatings.

This study serves to extend and complement previous investigations into crack formation, particularly investigating the effects of changing film thickness on crack spacing through a trio of methodologies.^{37,39} with the aim that these cracks can be designed into processes for microfluidics and MEMS. Film thickness will be varied through deposition speed, applied thermal gradients, and particle volume fraction. In addition, significant particle deformation comes into play in the formation of latex films—this work will present complementary data of silica nanoparticles, with an emphasis on the comparison of crack spacing between the two chemistries. The use of oxide nanoparticles should remove some limitations and complexities. In addition, previous research into the cracking of nanoparticle thin films has primarily concerned the evaporation of pools of suspensions—this shares strong parallels with droplet evaporation and the “coffee ring effect.” The use of convective deposition, where a suspension meniscus is pulled across a substrate, with particles drawn to an evaporative front and liquid thin film, enables significantly enhanced process control. In particular, this work will evaluate the transitions in cracking morphology with increasing, as well as decreasing, thin film thickness. The Clausius-Clapeyron relation enables an understanding of the use of applied thermal gradients in convective deposition. With regards to convective deposition, the inherent temperature component of this relation will directly affect vapor pressure in the suspension meniscus.

Materials and methods

Suspension Preparation:

The primary colloid suspension used in this work is prepared by dispersing SiO₂ and Polystyrene (PS) nanoparticles, of comparable size, in deionized (DI) water with a volume fraction ϕ_{nano} . The suspension is dispersed using a sonic dismembrator (model 550, Fisher Scientific, Pittsburgh, PA) for 10 min and then vortexed prior to coating. (Fisher Scientific, model 550). 80 nm SiO₂ nanoparticles are prepared through Stöber synthesis, paralleling the experimental techniques previously described.²¹ 75 nm PS nanoparticles are prepared by emulsion polymerization and supplied by the Emulsion Polymers Institute.

Substrate Preparation:

Plain glass microslides (76 × 25 × 1 mm³, Fisher PA) are used as deposition blades, and glass coverslips (60 × 24 × 0.25 mm³, Fisher PA) are used as substrates for all samples. All glassware is cleaned by immersion in Piranha solution, 5:1 v/v sulfuric acid/hydrogen peroxide, for 30 min. The cleaned glassware is rinsed with DI water until no residual acid remains and is then immersed in DI water until use. The bottom edge of the glass deposition blade is made hydrophobic with a thin coating of parafilm (Fisher PA).

Convective Deposition of Particle Suspensions:

Under convective deposition, particles flow to the leading edge of the meniscus via evaporative forces, and are drawn to the three-phase contact line near the thin film region.

As particles flow into this thin film region, they are deposited and can form highly-crystalline structures through capillary interactions. Convective deposition experiments are carried out as shown previously.²⁰ A suspension meniscus is pinned atop a glass substrate, by a hydrophobically-coated deposition blade. A linear motor is used to translate the substrate and draw out a thin film. The volume of colloid suspension for each experiment is 10 μL . As an enhancement, some experiments are performed atop a Fisher Scientific isotemp stirring hot plate. Note that surface temperatures noted are hot plate set points. This increases film thickness by increasing evaporation flux.

Microstructural Analysis:

Deposited monolayers are observed directly using scanning electron microscopy (SEM) and confocal laser scanning microscopy. A Hitachi 4300 field emission SEM is used to observe particle array microstructure. Prior to SEM imaging, the sample is coated with iridium by vapor deposition. Optical and confocal microscopy is performed using an Olympus IX71 optical microscope paired with a Visitech VTEye confocal system, in conjunction with a 100x objective. Confocal laser scanning microscopy (VTEye, Visitech International) is used to observe the microstructure after rewetting the layer with an aqueous solution of 8 mM Rhodamine B for imaging; this rewetting does not alter the microstructure. Profilometry is carried out using a Zygo Zometrics ZeGAGE Interference Profilometer, with a 10x objective. Image analysis of optical and electron microscope imagery, as well as interference profilometer, data were carried out using ImageJ.

As shown in Figure 1, convective deposition is used to induce the formation of cracks with highly monodisperse spacing. Cracks spacing is tuned by changing the coating thickness. The suspension from bulk meniscus is dragged towards the drying thin

film (figure1a). Particles then assemble themselves at the packing front and liquid flows through this porous media to compensate for the evaporative loss. Compressive stresses developed due to capillary forces result in formation of cracks. Note how uniform cracks spacing can be obtained over large scales compared with irregular drying in a Petri dish.

A trio of methodologies is used to control nanoparticle thin film thickness, with increased thickness yielding larger crack spacing. Coating thickness is first tuned via suspension volume fraction, with higher volume fractions generating thicker films. Likewise, the evaporative flux can be increased by heating the substrate, increasing coating thickness. Finally, deposition speed, the speed at which the suspension is dragged across the substrate, will tune sample thickness. In these batch experiments, a single volume fraction and thermal gradient are applied to each sample. Thus thin films of homogeneous thickness are deposited. Contrastingly, deposition speed can be varied throughout a batch coating in order to systematically vary thin film thickness. Increasing nanoparticle thin film thickness, via slower deposition speeds, applied thermal gradients, or increased volume fraction, will limit sample transparency. There is small variation in cracks spacing, thus the measurement is done by averaging over ten cracks. The standard deviation is small but must be taken into account while fabricating devices.

Results and discussions

Film thickness and crack spacing

Previous data do not address small scale cracking and thinner particle coatings as a result of experimental limitations.³⁷ Interference profilometry, in correlation with high

resolution optical microscopy, are used to expand established film thickness to crack spacing relations over small length scales. These techniques provide micron to submicron-level detail. The coating thickness was measured by using bare glass slide as a reference point in interference profilometry. Samples were scratched by fine blade to remove particles near particular measurement area to access the reference height. Figure 2a provides a presentation of crack spacing data with thin film thickness the film thickness is varied by changing substrate velocity between 32 $\mu\text{m/s}$ to 64 $\mu\text{m/s}$. Previous data support this trend with power law scaling (figure 2b).³⁷ These experimental relations clearly parallel the theory (1) through (5) where a clear linear trend between relevant hydrodynamic length scale and crack spacing is expected. Also, note that a minimum crack spacing of $\sim 2 \mu\text{m}$ is presented in figure 2. That is the minimum observed spacing where cracks show significant length and monodisperse spacing. Below that length scale, the analysis becomes increasingly complex as samples are characterized by small-scale subcracks. It is important to note that these thinnest films, and the disappearance of cracking, are on the order of 15-25 particle layers thick. On these length scales particle-particle interactions and capillary forces become increasingly significant versus large scale thin film evaporative hydrodynamics.

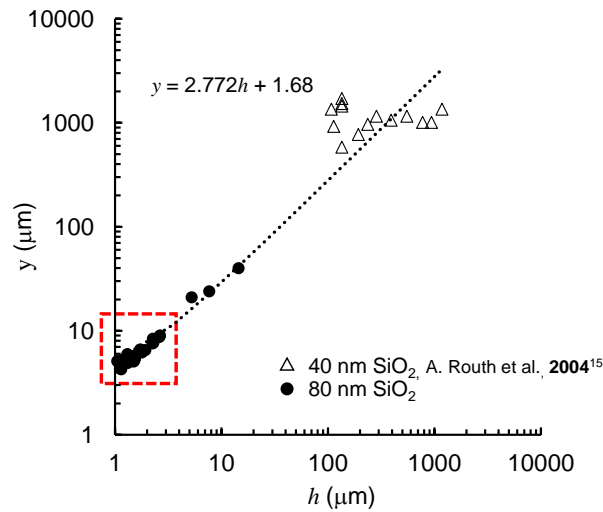
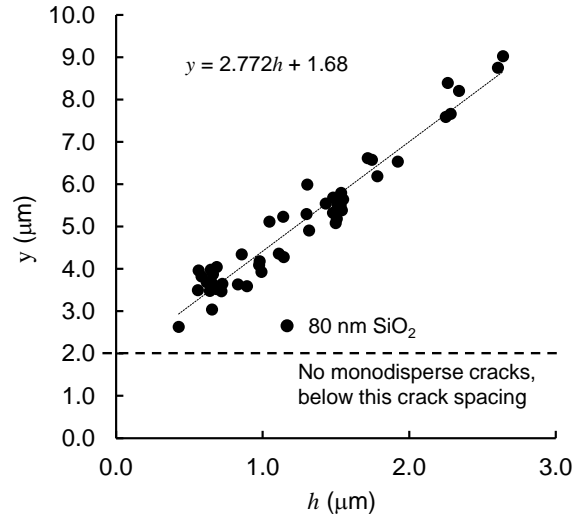


Figure 2: a) Crack spacing vs film thickness obtained at much smaller film thickness, b) comparing the data at lower coating thickness (dark circles) with A. Routh existing data at much larger thickness (open triangles). The red dotted square in 2b is representing the same data from 2a.

Hydrodynamic Scaling

Paralleling the work of Routh et al., 2004, the correlation of crack spacing with thickness can be further examined with the addition of hydrodynamic scaling.³⁷ Crack spacing, y , normalized by the horizontal hydrodynamic scaling, X , (4), is plotted with P_{cap} (5).

Routh et al., 2004 found their data collapsed along the trend:

$$\frac{y}{X} = 0.07 P_{cap}^{-0.8} \quad (7)$$

Figure 3 presents the trend of Routh et al., 2004 alongside the hydrodynamically scaled data in this study. The data donot quite match with $0.07.P_{cap}^{-0.8}$, this can be attributed to different characteristic velocity in convective deposition. Since the substrate is moving as the porous media with u_s , the characteristic fluid velocity depends not only on evaporation rate J_e but also u_s .

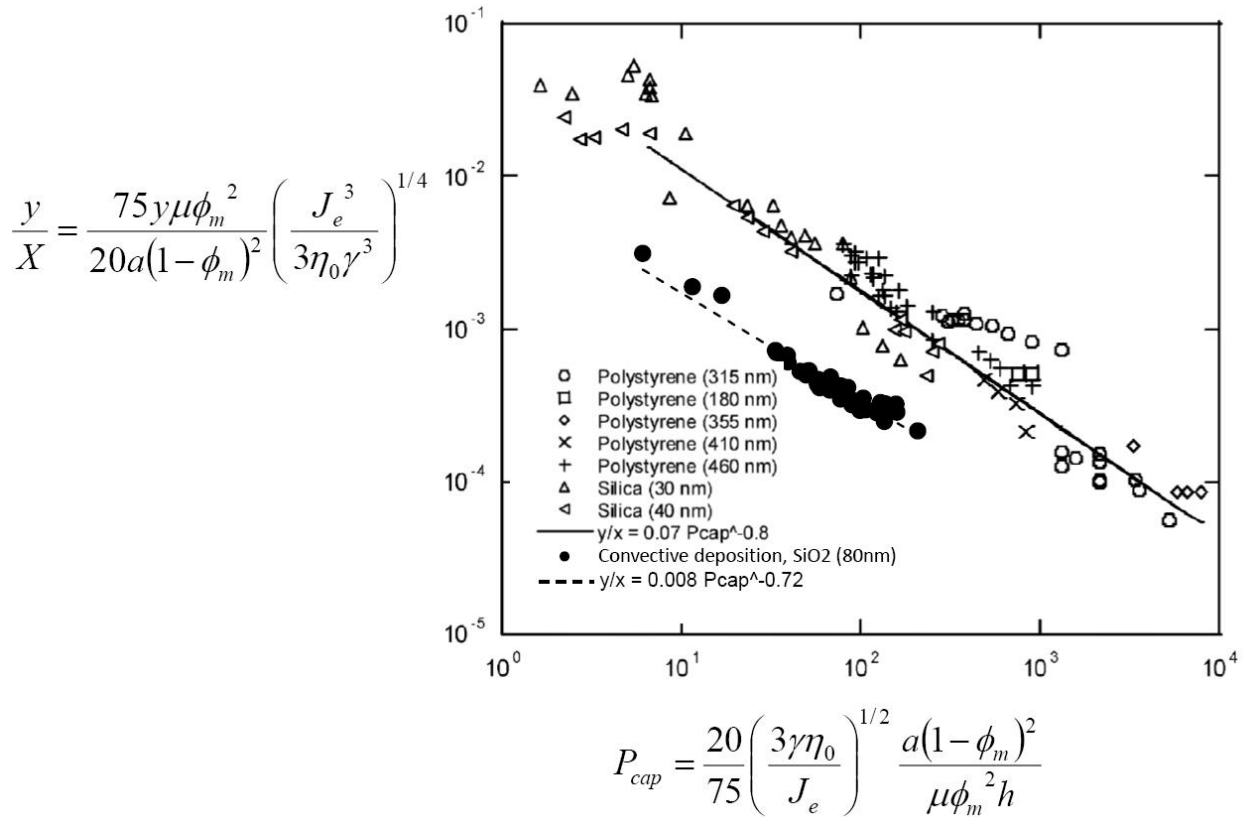


Figure 3 Crack spacing, y , hydrodynamically scaled by X , versus capillary pressure. Routh et al., 2004 data is shown in top trend, as $y/X = 0.07P_{cap}^{-0.8}$. Lower data and trend show this study's data, under smaller scale cracked thin films the data best fit to $y/X = 0.008P_{cap}^{-0.72}$.

Evaporation flux and crack spacing

From the equations above, evaporation plays complementary strong roles in the formation of cracks, through evaporation rate, J_e . One method by which evaporate rate and flux will be controlled is through the application of applied thermal gradients. The Clausius-Clapeyron relation enables an understanding of the use of applied thermal gradients in convective deposition. With regards to convective deposition, the inherent temperature component of this relation will directly affect vapor pressure in the suspension meniscus.

The characteristic fluid velocity, u , relaxation length scale, X , and dimensionless capillary pressure, P_{cap} , are all a function of dried film thickness, h . An increased vapor pressure in the system will in turn force additional liquid into the vapor phase. Thusly the evaporative flux will increase. Increased evaporative flux near the three-phase contact will increase fluid and particle convection to the evaporative front. Keeping other experimental parameters static, increased particle flow into the thin film region will correlate with an increased thin film thickness, in terms of number of particle layers n , an increased number of particle layers in the resultant coating will increase the film height h . Finally, as previously shown in Eq. 6, the film thickness scales inversely with deposition speed.

$$e^{\frac{-\Delta H_v}{RT}} \propto p^* \propto J_e \propto n \propto h \propto u^{-1} \quad (8)$$

In conclusion, the inverse of temperature, as an applied thermal gradient in these experiments, will scale with deposition speed $\langle e^{1/T} \propto u \rangle$. Either increased applied thermal gradients or decreased deposition speed will increase thin film thickness. Under alternative experimental parameters these same principles can also be used to spur instabilities and recirculation in convective deposition, as well as the assembly of macroscale coating defects.

Figure 4 presents a more extensive comparison, with film thickness, and crack spacing, controlled through an applied thermal gradient. This applied thermal gradient changes the evaporative flux of the system, and data will be presented in terms of a relative evaporative flux versus ambient conditions. Evaporative flux is proportional to partial pressure.

Data is presented in terms of relative evaporative flux, where all higher-temperature (t) conditions are normalized by the ambient (t^*) temperature. Partial pressure p is defined as $(v_p * RH / 100)$ where, RH is relative humidity which was kept constant in all cases.

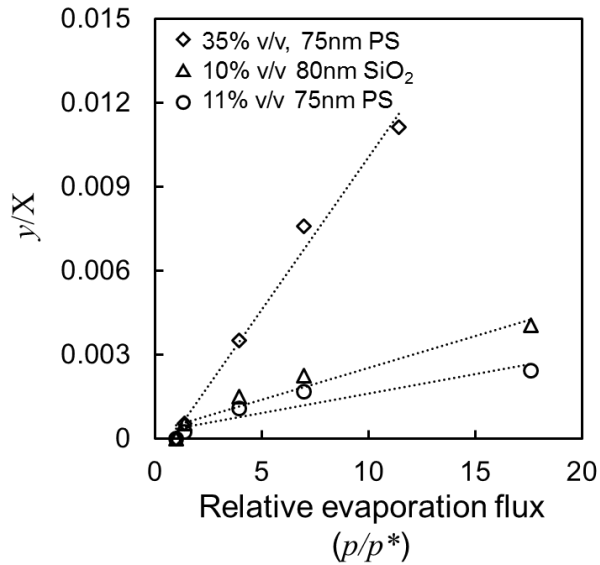


Figure 4 crack spacing y as a function of relative evaporation flux. p/p^* is partial pressure at experimental conditions over partial pressure at room temperature. Crack spacing in SiO₂ and PS thin films as deposited through convective deposition. Diamonds represent 35 vol. % 75 nm PS suspensions, triangles represent 10 vol. % 80 nm SiO₂ suspensions, and circles represent 11 vol. % 75 nm PS suspensions. Thus SiO₂ and PS particles are of comparable size. Crack spacing is controlled through increasing evaporative flux. All suspensions were deposited at 41.7 $\mu\text{m}/\text{sec}$.

Note the very similar trends in crack spacing with comparable SiO₂ and PS suspension and processing characteristics, as shown in the triangles and circles of figure 4. The “softer” PS particles do exhibit slightly smaller crack spacing, but both systems show highly controlled thin film morphology. The differences are subtle, and could also be due to minute differences in particle size and volume fraction. The fact that both systems show parallel cracking characteristics validates the following studies. Polystyrene and SiO₂ data will be presented in the forthcoming results.

Figure 4 also allows experimental parameters to be probed via changes in suspension volume fraction. 11% and 35% (v/v) PS suspensions, circles and diamonds markers respectively, are deposited with constant processing parameters. Again, a hot

plate is used to apply a thermal gradient to the drying thin film and thus increase crack spacing. As expected, higher suspension volume fraction yields thicker nanoparticle coatings. Also, it is important to note that the absence of data under ambient temperature conditions, 23°C, is due to a complete absence of cracking.

Deposition Speed as a Method to Probe Transitions in Crack Spacing

This final section aims to probe and explain transitioning crack spacing with changing coating thickness. Deposition speed can be increased or decreased. These speed changes result in changing the film thickness and crack spacing. Figure 5 provides data on variable speed coatings and highlights changing crack width and transition regions. This sample is initially thin (Figure 5a), and is subject to sequentially increasing thickness over regions of equal length. Upon reaching a prescribed thickness, deposition speed is increased to again thin the sample.

This coating starts and ends under fast enough deposition speeds so as not to exhibit cracks or significant large-scale crystalline defects (Figure 5a,5d). Upon reaching a critical thickness, cracks arise in a uniform front (Figure 5a). Crack spacing reaches a steady state value, in a 5.1 μm thick film, of 15 μm . In the transition to a much thicker film, 14.7 μm as estimated via the fitting from Figure 3, there is a stark change in thickness and crack spacing (Figure 5b). Note the initial delamination at this transition point. Under these thicker conditions, crack spacing reaches a steady state value of 40 μm .

Next, the thinning condition will be presented (Figure 5c-d). The transition from 14.7 μm thickness exhibits significant stick-slip motion initiated by the change in velocity (Figure 5c). Stick-slip motion refers to the periodic pinning and depinning of the meniscus to the substrate that can result in significant nonuniformities in the coating during drying

of suspensions^{63,64}. Here, crack spacing periodically varies between a larger and smaller value in the deposition direction, and also exhibits some lateral nonuniformities. Note that these increases and decreases in crack spacing do in fact correlate with increasing and decreasing film thickness, as confirmed by interference profilometry. Stick-slip motion subsides and thin film morphology reaches steady state thickness of 3.5 μm . Crack spacing reaches a uniform value of 11 μm . Note that this film is slightly thinner than the parallel condition presented in Figure 5a—this difference is attributed to suspension depletion. In the transition from a 3.5 μm film thickness to the “crack-less” condition, significant “stick-slip” motion is observed, with correlative changes in crack spacing (Figure 5d). Again, under the fastest deposition speed yielding relatively thin films, coatings do not exhibit cracking. It is important to note that stick-slip motion is observed under both thinning (Figure 5c-d) and thickening (Figure 5a-b) conditions. However, qualitatively, more exaggerated stick-slip transition regions are seen under thinning conditions, where coating speed is increased.

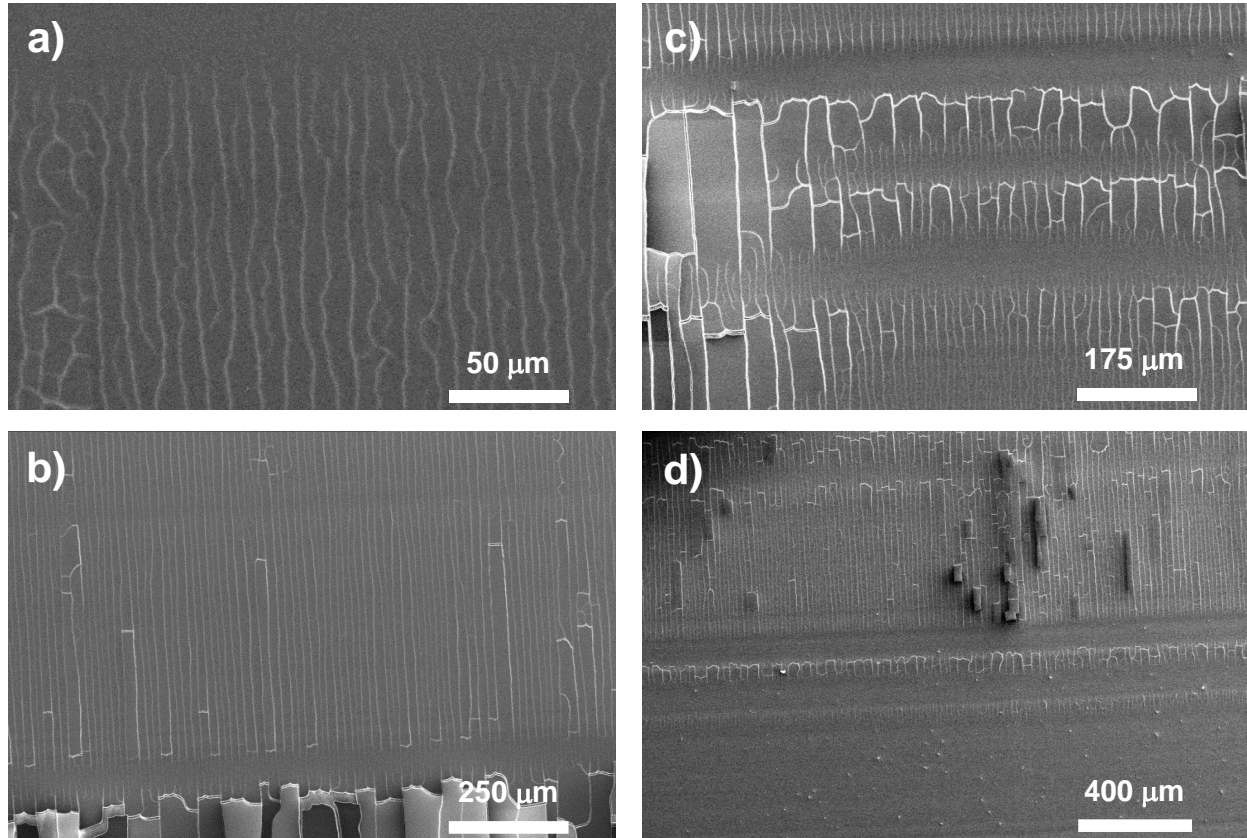


Figure 5 Scanning electron microscope images showing a, b) increases and c, d) decreases in crack spacing with changing film thickness (via deposition speed). These data highlight transition regions in particular. Especially in the thinning condition (c-d), with increasing deposition speed, stick-slip motion is observed, where crack spacing periodically varies. Both thinning and thickening conditions also highlight the absence of cracking under sufficiently thin conditions. Note that, as calculated through profilometry data as presented in Figure 3, the steady-state thickness are: 5a (5.1 μm), 5b (5.1 to 14.7 μm), 5c (14.7 to 3.5 μm), 5d (3.5 μm).

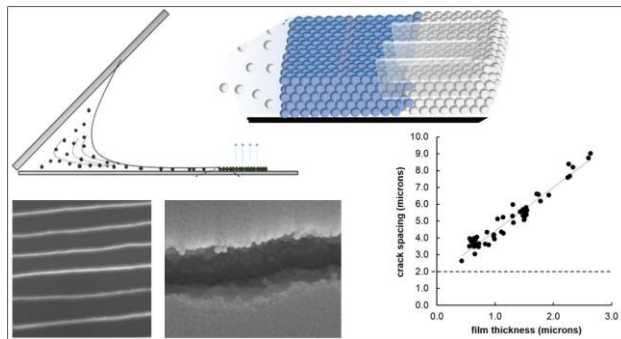
Conclusion

This work concerns deposited nanoparticle thin films and the ability to tune the formation of longitudinal cracking with highly uniform spacing that could be used in microfluidics or MEMS. Increased coating thickness correlates with the onset and increased spacing between micro- to macroscale cracks. Coating thickness is varied through deposition speed, applied thermal gradients, and suspension volume fraction. In a significant process enhancement versus previous work, coating thickness is varied within individual experiments. This analysis from a batch to semi-batch methodology enables previously unattainable analysis of transition regions, in particular these results highlight the onset of stick-slip variability with changing coating thickness. Next steps include complementary in-situ experiments to quantify crack formation mechanisms and timescales. This will complement the work of Routh et al.^{30,39}, who by changing the timescales of evaporation and re-wetting latex films, cyclically control the formation and suppression of individual and aggregate cracks. They demonstrate enormous plasticity in crack formation and evolution. Parallel experiments could be performed via in-situ confocal and optical microscopy, as well as interference profilometry.

Acknowledgements

We gratefully acknowledge initial conversations with A. Jagota. In addition, we acknowledge support from the National Science Foundation Scalable Nanomanufacturing Program under Grant No. 1120399.

TOC image



References

- (1) Routh, A. F. Drying of Thin Colloidal Films. *Reports Prog. Phys.* **2013**, 76 (4), 046603.
- (2) Routh, A. F.; Zimmerman, W. B. Distribution of Particles during Solvent Evaporation from Films. *Chem. Eng. Sci.* **2004**, 59 (14), 2961–2968.
- (3) Joy, M.; Muangnapoh, T.; Snyder, M. a; Gilchrist, J. F. Flow-Induced Alignment of (100) Fcc Thin Film Colloidal Crystals. *Soft Matter* **2015**, 11 (36), 7092–7100.
- (4) Im, S. H.; Lim, Y. T.; Suh, D. J.; Park, O. O. Three-Dimensional Self-Assembly of Colloids at a Water-Air Interface: A Novel Technique for the Fabrication of Photonic Bandgap Crystals. *Adv. Mater.* **2002**, 14 (19), 1367–1369.
- (5) Kumnorkaew, P.; Ee, Y. K.; Tansu, N.; Gilchrist, J. F. Investigation of the Deposition of Microsphere Monolayers for Fabrication of Microlens Arrays. *Langmuir* **2008**, 24 (21), 12150–12157.
- (6) Tessier, P. M.; Velev, O. D.; Kalambur, a. T.; Lenhoff, a. M.; Rabolt, J. F.; Kaler,

- E. W. Structured Metallic Films for Optical and Spectroscopic Applications via Colloidal Crystal Templating. *Adv. Mater.* **2001**, *13* (6), 396–400.
- (7) Haes, A. J.; Haynes, C. L.; Van Duyne, R. P. Nanosphere Lithography: Self-Assembled Photonic and Magnetic Materials. *MRS Proc.* **2000**, *636*, 1–6.
- (8) Vlasov, Y. a; Bo, X. Z.; Sturm, J. C.; Norris, D. J. On-Chip Natural Assembly of Silicon Photonic Bandgap Crystals. *Nature* **2001**, *414* (6861), 289–293.
- (9) Johnson, N. P.; Jin, C.; Li, Z. Y.; McLachlan, M. A.; McComb, D. W.; De La Rue, R. M. Optical Properties of Tetragonal Photonic Crystal Synthesized via Template-Assisted Self-Assembly. *J. Appl. Phys.* **2006**, *99* (11).
- (10) Harris, D. J.; Hu, H.; Conrad, J. C.; Lewis, J. a. Patterning Colloidal Films via Evaporative Lithography. *Phys. Rev. Lett.* **2007**, *98* (14), 1–4.
- (11) Haynes, C. L.; McFarland, A. D.; Zhao, L.; Van Duyne, R. P.; Schatz, G. C.; Gunnarsson, L.; Prikulis, J.; Kasemo, B.; Käll, M. Nanoparticle Optics: The Importance of Radiative Dipole Coupling in Two-Dimensional Nanoparticle Arrays †. *J. Phys. Chem. B* **2003**, *107* (30), 7337–7342.
- (12) Biancaniello, P. L.; Crocker, J. C. Line Optical Tweezers Instrument for Measuring Nanoscale Interactions and Kinetics. *Rev. Sci. Instrum.* **2006**, *77* (11), 1–10.
- (13) Hayward, R. C.; Saville, D. a; Aksay, I. a. Electrophoretic Assembly of Colloidal Crystals with Optically Tunable Micropatterns. *Nature* **2000**, *404* (6773), 56–59.
- (14) Koyama, K.; Yamaguchi, N.; Miyasaka, T. Antibody-Mediated Bacteriorhodopsin Orientation for Molecular Device Architectures. *Science (New York, N. Y.)*. 1994, pp 762–765.
- (15) Velev, O. D.; Kaler, E. W. In Situ Assembly of Colloidal Particles into Miniaturized

- Biosensors. *Langmuir* **1999**, *15* (11), 3693–3698.
- (16) Yi, D. K.; Kim, M. J.; Turner, L.; Breuer, K. S.; Kim, D. Y. Colloid Lithography-Induced Polydimethylsiloxane Microstructures and Their Application to Cell Patterning. *Biotechnol. Lett.* **2006**, *28* (3), 169–173.
- (17) Wang, B.; L. Weldon, A.; Kumnorkaew, P.; Xu, B.; Gilchrist, J. F.; Cheng, X. Effect of Surface Nanotopography on Immunoaffinity Cell Capture in Microfluidic Devices. *Langmuir* **2011**, *27* (17), 11229–11237.
- (18) Han, W.; Allio, B. a.; Foster, D. G.; King, M. R. Nanoparticle Coatings for Enhanced Capture of Flowing Cells in Microtubes. *ACS Nano* **2010**, *4* (1), 174–180.
- (19) Tuttle, P. V; Rundell, a E.; Webster, T. J. Influence of Biologically Inspired Nanometer Surface Roughness on Antigen-Anti Body Interactions for Immunoassay-Biosensor Applications. *Int. J. Nanomedicine* **2006**, *1* (4), 497–505.
- (20) Hughes, A. D.; King, M. R. Use of Naturally Occurring Halloysite Nanotubes for Enhanced Capture of Flowing Cells. *Langmuir* **2010**, *26* (14), 12155–12164.
- (21) Weldon, A. L.; Kumnorkaew, P.; Wang, B.; Cheng, X.; Gilchrist, J. F. Fabrication of Macroporous Polymeric Membranes through Binary Convective Deposition. *ACS Appl. Mater. Interfaces* **2012**, *4* (9), 4532–4540.
- (22) Boudreau, L. C.; Kuck, J. a.; Tsapatsis, M. Deposition of Oriented Zeolite A Films: In Situ and Secondary Growth. *Journal of Membrane Science*. 1999, pp 41–59.
- (23) Bohaty, A. K.; Abelow, A. E.; Zharov, I. Nanoporous Silica Colloidal Membranes Suspended in Glass. *J. Porous Mater.* **2010**, *18* (3), 297–304.
- (24) Yuan, Z.; Burckel, D. B.; Atanassov, P.; Fan, H. Convective Self-Assembly to Deposit Supported Ultra-Thin Mesoporous Silica Films. *J. Mater. Chem.* **2006**, *16*

- (48), 4637.
- (25) Velev, O. D.; Lenhoff, A. M. Colloidal Crystals as Templates for Porous Materials T. *Synthesis (Stuttg)*. **2000**, 5, 56–63.
- (26) Zhang, Y.; Wang, S.; Eghtedari, M.; Motamedi, M.; Kotov, N. a. Inverted-Colloidal-Crystal Hydrogel Matrices as Three-Dimensional Cell Scaffolds. *Adv. Funct. Mater.* **2005**, 15 (5), 725–731.
- (27) Pawar, A. B.; Kretzschmar, I. Patchy Particles by Glancing Angle Deposition. *Langmuir* **2008**, 24 (2), 355–358.
- (28) Pawar, A. B.; Kretzschmar, I. Fabrication, Assembly, and Application of Patchy Particles. *Macromol. Rapid Commun.* **2010**, 31 (2), 150–168.
- (29) Paunov, V. N.; Cayre, O. J. Supraparticles and “Janus” Particles Fabricated by Replication of Particle Monolayers at Liquid Surfaces Using a Gel Trapping Technique. *Adv. Mater.* **2004**, 16 (910), 788–791.
- (30) Lee, W. P.; Routh, A. F. Time Evolution of Transition Points in Drying Latex Films. *J. Coatings Technol. Res.* **2006**, 3 (4), 301–306.
- (31) Kim, H.-N.; Lee, S.-H.; Suh, K.-Y. Controlled Mechanical Fracture for Fabricating Microchannels with Various Size Gradients. *Lab Chip* **2011**, 11 (4), 717–722.
- (32) Atwater, H. A.; Polman, A. Plasmonics for Improved Photovoltaic Devices. *Nat. Mater.* **2010**, 9 (10), 865–865.
- (33) Saracut, V.; Gilman, M.; Gabor, M.; Astilean, S.; Farcau, C. Polarization-Sensitive Linear Plasmonic Nanostructures via Colloidal Lithography with Uniaxial Colloidal Arrays. *ACS Appl. Mater. Interfaces* **2013**, 5 (4), 1362–1369.
- (34) Han, W.; Li, B.; Lin, Z. Drying-Mediated Assembly of Colloidal Nanoparticles into

- Large-Scale Microchannels. *ACS Nano* **2013**, 7 (7), 6079–6085.
- (35) Routh, A. F.; Russel, W. B. Deformation Mechanisms during Latex Film Formation: Experimental Evidence. *Ind. Eng. Chem. Res.* **2001**, 40, 4302–4308.
- (36) Lee, W. P.; Routh, A. F. Why Do Drying Films Crack? *Langmuir* **2004**, 20 (23), 9885–9888.
- (37) Lee, W. P.; Routh, A. F. Temperature Dependence of Crack Spacing in Drying Latex Films. *Ind. Eng. Chem. Res.* **2006**, 45, 6996–7001.
- (38) Goehring, L.; Clegg, W. J.; Routh, A. F. Plasticity and Fracture in Drying Colloidal Films. *Phys. Rev. Lett.* **2013**, 110 (2), 1–5.
- (39) Yow, H. N.; Goikoetxea, M.; Goehring, L.; Routh, A. F. Effect of Film Thickness and Particle Size on Cracking Stresses in Drying Latex Films. *Journal of colloid and interface science*. 2010, pp 542–548.
- (40) Petersen, C.; Heldmann, C.; Johannsmann, D. Internal Stresses during Film Formation of Polymer Latices. *Langmuir* **1999**, No. 11, 7745–7751.
- (41) Dragnevski, K. I.; Routh, A. F.; Murray, M. W.; Donald, A. M. Cracking of Drying Latex Films.pdf. *Langmuir* **2010**, 110, 0243301–1 – 0243301.
- (42) Dufresne, E. R.; Corwin, E. I.; Greenblatt, N. a; Ashmore, J.; Wang, D. Y.; Dinsmore, a D.; Cheng, J. X.; Xie, X. S.; Hutchinson, J. W.; Weitz, D. a. Flow and Fracture in Drying Nanoparticle Suspensions. *Phys. Rev. Lett.* **2003**, 91 (November), 224501.
- (43) Wang, D. Y.; Mohwald, H. Rapid Fabrication of Binary Colloidal Crystals by Stepwise Spin-Coating. *Adv. Mater.* **2004**, 16 (3), 244–247.
- (44) Vozar, S.; Poh, Y. C.; Serbowicz, T.; Bachner, M.; Podsiadlo, P.; Qin, M.;

- Verploegen, E.; Kotov, N.; Hart, A. J. Automated Spin-Assisted Layer-by-Layer Assembly of Nanocomposites. *Rev. Sci. Instrum.* **2009**, *80* (2), 3–7.
- (45) Toolan, D. T. W.; Fujii, S.; Ebbens, S. J.; Nakamura, Y.; Howse, J. R. On the Mechanisms of Colloidal Self-Assembly during Spin-Coating. *Soft Matter* **2014**, *10* (44), 8804–8812.
- (46) Ye, R.; Ye, Y. H.; Zhou, Z.; Xu, H. Gravity-Assisted Convective Assembly of Centimeter-Sized Uniform Two-Dimensional Colloidal Crystals. *Langmuir* **2013**, *29* (6), 1796–1801.
- (47) Qian, F.; Pascall, A. J.; Bora, M.; Han, T. Y. J.; Guo, S.; Ly, S. S.; Worsley, M. A.; Kuntz, J. D.; Olson, T. Y. On-Demand and Location Selective Particle Assembly via Electrophoretic Deposition for Fabricating Structures with Particle-to-Particle Precision. *Langmuir* **2015**, *31* (12), 3563–3568.
- (48) Velev, O. D.; Bhatt, K. H. On-Chip Micromanipulation and Assembly of Colloidal Particles by Electric Fields. *Soft Matter* **2006**, *2* (9), 738.
- (49) Prevo, B. G.; Kuncicky, D. M.; Velev, O. D. Engineered Deposition of Coatings from Nano- and Micro-Particles: A Brief Review of Convective Assembly at High Volume Fraction. *Colloids Surfaces A Physicochem. Eng. Asp.* **2007**, *311* (1-3), 2–10.
- (50) Dimitrov, A. S.; Nagayama, K. Continuous Convective Assembling of Fine Particles into Two-Dimensional Arrays on Solid Surfaces. *Langmuir* **1996**, *12* (5), 1303–1311.
- (51) Shimmin, R. G.; DiMauro, A. J.; Braun, P. V. Slow Vertical Deposition of Colloidal Crystals: A Langmuir-Blodgett Process? *Langmuir* **2006**, *22* (15), 6507–6513.
- (52) Diao, J. J.; Hutchison, J. B.; Luo, G.; Reeves, M. E. Theoretical Analysis of Vertical

- Colloidal Deposition. *J. Chem. Phys.* **2005**, *122* (18), 184710.
- (53) Vella, D.; Mahadevan, L. The “Cheerios Effect.” *Am. J. Phys.* **2005**, *72* (817).
- (54) Xiao, J.; Bhardwaj, R.; Attinger, D. Manufacturing Self-Assembled Coatings of Micro- and Nano-Particles by Controlled Evaporation of Drops and Thin Films. *SPIE* **2011**, *8031* (April), 80310–80310 – 11.
- (55) Luo, H.; Cardinal, C. M.; Scriven, L. E.; Francis, L. F. Ceramic Nanoparticle/Monodisperse Latex Coatings. *Langmuir* **2008**, *24* (10), 5552–5561.
- (56) Prevo, B. G.; Fuller, J. C.; Velev, O. D. Rapid Deposition of Gold Nanoparticle Films with Controlled Thickness and Structure by Convective Assembly. *Chem. Mater.* **2005**, *17* (1), 28–35.
- (57) Brewer, D. D.; Allen, J.; Miller, M. R.; Santos, J. M. De; Kumar, S.; Norris, D. J.; Tsapatsis, M.; Scriven, L. E. Mechanistic Principles of Colloidal Crystal Growth by Evaporation-Induced Convective Steering. *Langmuir* **2008**, *24* (23), 13683–13693.
- (58) Prevo, B. G.; Velev, O. D. Controlled, Rapid Deposition of Structured Coatings from Micro- and Nanoparticle Suspensions. *Langmuir* **2004**, *20* (6), 2099–2107.
- (59) Dimitrov, A. S.; Nagayama, K. Steady-State Unidirectional Convective Assembling of Fine Particles into Two-Dimensional Arrays. *Chem. Phys. Lett.* **1995**, *243* (5-6), 462–468.
- (60) Kralchevsky, P. a.; Nagayama, K. Capillary Interactions between Particles Bound to Interfaces, Liquid Films and Biomembranes. *Adv. Colloid Interface Sci.* **2000**, *85* (2), 145–192.
- (61) Nagayama, K. Two-Dimensional Self-Assembly of Colloids in Thin Liquid Films. *Colloids Surfaces A Physicochem. Eng. Asp.* **1996**, *109*, 363–374.

- (62) Joshi, K.; Muangnapoh, T.; Stever, M. D.; Gilchrist, J. F. Effect of Ionic Strength and Surface Charge on Convective Deposition. *Langmuir* **2015**, *31* (45), 12348–12353.
- (63) Adamson, A. W.; Gast, A. P. *Physical Chemistry of Surfaces - 6th Edition*; 1997.
- (64) Deegan, R. D.; Bakajin, O.; Dupont, T. F.; Huber, G.; Nagel, S. R.; Witten, T. a. Contact Line Deposits in an Evaporating Drop. *Phys. Rev. E - Stat. Physics, Plasmas, Fluids, Relat. Interdiscip. Top.* **2000**, *62* (1 B), 756–765.